A coupled Immersed Boundary – Lattice Boltzmann method for incompressible flows through moving porous media A coupled Immersed Boundary -Lattice Boltzmann method for incompressible flows through moving porous media

Marianna Pepona, Julien Favier

▶ **To cite this version:**

Marianna Pepona, Julien Favier. A coupled Immersed Boundary – Lattice Boltzmann method for incompressible flows through moving porous media A coupled Immersed Boundary -Lattice Boltzmann method for incompressible flows through moving porous media. Journal of Computational Physics, 2016, 321, pp.1170-1184. 10.1016/j.jcp.2016.06.026 . hal-01336315

HAL Id: hal-01336315
https://hal.science/hal-01336315v1

Submitted on 23 Jun 2016

HAL is a multi-disciplinary open access archive for the deposit and dissemination of scientific research documents, whether they are published or not. The documents may come from teaching and research institutions in France or abroad, or from public or private research centers.

L'archive ouverte pluridisciplinaire **HAL**, est destinée au dépôt et à la diffusion de documents scientifiques de niveau recherche, publiés ou non, émanant des établissements d'enseignement et de recherche français ou étrangers, des laboratoires publics ou privés.

Accepted Manuscript

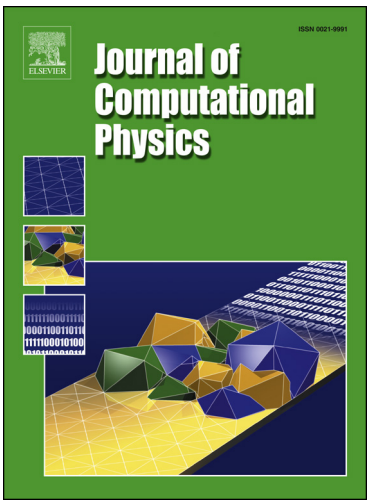

A coupled Immersed Boundary – Lattice Boltzmann method for incompressible flows through moving porous media

Marianna Pepona, Julien Favier

PII: S0021-9991(16)30251-0
DOI: http://dx.doi.org/10.1016/j.jcp.2016.06.026
Reference: YJCPH 6687

To appear in: *Journal of Computational Physics*

Received date: 26 January 2016
Revised date: 8 June 2016
Accepted date: 17 June 2016

Please cite this article in press as: M. Pepona, J. Favier, A coupled Immersed Boundary – Lattice Boltzmann method for incompressible flows through moving porous media, *J. Comput. Phys.* (2016), http://dx.doi.org/10.1016/j.jcp.2016.06.026

This is a PDF file of an unedited manuscript that has been accepted for publication. As a service to our customers we are providing this early version of the manuscript. The manuscript will undergo copyediting, typesetting, and review of the resulting proof before it is published in its final form. Please note that during the production process errors may be discovered which could affect the content, and all legal disclaimers that apply to the journal pertain.

ACCEPTED MANUSCRIPT

A coupled Immersed Boundary - Lattice Boltzmann method for incompressible flows through moving porous media

Marianna Pepona[a], Julien Favier[a]

[a]*Aix Marseille Université, CNRS, Centrale Marseille, M2P2 UMR 7340, 13451, Marseille, France*

Abstract

In this work, we propose a numerical framework to simulate fluid flows in interaction with moving porous media of complex geometry. It is based on the Lattice Boltzmann method including porous effects via a Brinkman-Forchheimer-Darcy force model coupled to the Immersed Boundary method to handle complex geometries and moving structures. The coupling algorithm is described in detail and it is validated on well-established literature test cases for both stationary and moving porous configurations. The proposed method is easy to implement and efficient in terms of CPU cost and memory management compared to alternative methods which can be used to deal with moving immersed porous media, e.g. re-meshing at each time step or use of a moving/chimera mesh. An overall good agreement was obtained with reference results, opening the way to the numerical simulation of moving porous media for flow control applications.

Keywords: Lattice Boltzmann method, Immersed Boundary method, moving porous medium, poroelastic coating

1. Introduction

Fluid flows in porous media is a research topic of growing interest due to its numerous applications in chemical or oil engineering [1, 2, 3], but also in other areas such as biological flows or even aeronautics, where coatings made of porous materials are more and more considered for flow control applications [4]. Indeed controlling the flow using a porous coating, or a porous actuator, has been tested in previous literature studies and showed to yield a positive effect on the aerodynamic performances of immersed bluff bodies [5]. The present work is motivated by a potential use in aeronautical applications of a porous coating, which would have a moving feature, i.e. would be capable of adapting its shape to the flow topology to promote drag-reducing and lift-enhancement properties. This breakthrough and novel technology for flow control actuators has recently showed a promising potential [6], but there actually exist several issues in terms of numerical modelling. The main challenge is to model numerically a moving

ACCEPTED MANUSCRIPT

or deformable porous medium interacting with a fluid flow at reasonable CPU costs. Another interesting feature related to flow control applications is to be able to simulate a porous medium of complex geometry (not aligned with the mesh) for noise control applications.

For the applications we are targeting, solving the fluid flow at the porous scale is generally costly and associated to prohibitive CPU costs because of the number of points required to resolve the pores. To overcome this issue, the so-called Representative Elementary Volume (REV) scale is adopted in the present work. It consists of a control volume defined in the porous medium, of size much larger than the pore scale, and much smaller than the characteristic scale of the macroscopic problem [7]. At the REV scale, the porous medium can be seen as a continuum and the fluid properties defined over that volume are assumed to remain constant (density, velocity etc.). Moreover, the flow can be characterized by empirical models such as Darcy's law, stating that the velocity through the porous medium is proportional to the pressure gradient. By choosing not to resolve the flows at the pore scale, we are thus in this work resolving the momentum equations averaged at the REV scale, for a fluid described by some global properties such as porosity and permeability.

To solve the flow equations, we choose to use the Lattice Boltzmann Method (LBM), which is particularly interesting for porous flows as it is relatively straightforward to implement in the formalism various empirical macroscopic models defined at the REV scale. Other advantages of using LBM include the good parallelisation properties of the solver (due to the locality of the algorithm) and the capability of adding relatively easily new physics to the model (multiphase, etc.).

In literature, the first attempts to model porous media with LBM date back to the Dardis-McCloskey model [8] based on pore scale. Almost at the same time, [9] propose a formalism based on LBM at the REV scale, inspired by the treatment of the pseudo-potential force in the Shan-Chen model for multiphase flows [10]: the velocity is modified by a body force, mimicking the medium resistance to the flow by a Darcy's law, which then in turn modifies the equilibrium function. These two approaches are actually solving the Brinkman equation, and suffer from limitations related to the use of a simple force term to model porous effects. To extend the model beyond Darcy and Brinkman laws, [11] propose to include an extra term to take into account the non-linear resistance of the medium : the Forchheimer term. This model takes the name of generalised Lattice Boltzmann model, as it can be shown using the Chapman Enskog analysis [12] in the incompressible limit that it is equivalent to solving the generalised Navier Stokes equations given at §2.1. In this work we simulate stationary porous objects using the model proposed by [12], while the model of [13] is used for moving porous bodies.

The applications related to flow control using shape-adapting porous coating or porous coating of complex geometry require the resolution of the coupled dynamics of structure and fluid. To avoid the prohibitive solution of remeshing at each iteration the fluid domain as a function of the structure position, we adopt here an approach based on Immersed Boundary Method (IBM) which consists

ACCEPTED MANUSCRIPT

in treating in one shot both the fluid momentum equations and the imposition of unsteady boundary conditions at the porous walls. Originally proposed by [14] the IBM approach is designed to simulate fluid flows interacting with solid bodies. It consists in treating the fluid domain in an Eulerian fashion on a fixed mesh, and the moving structure in a Lagrangian fashion using moving Lagrangian markers. The same set of equations is solved in both the fluid and solid domain, and the boundary condition at the wall is imposed via a system of singular boundary forces. The interesting feature in the context of the applications considered in this work is the capability of positioning Lagrangian markers which do not coincide with the underlying fluid Eulerian nodes. The IBM has evolved rapidly over the last decades and has been successfully implemented in LBM solvers [15, 16, 17, 18]. In this work we use a formulation proposed in [18], adapted to porous flows by defining the porous forces on each Lagrangian marker.

To the knowledge of the authors, there is no literature work which addresses completely the problem of a moving porous medium immersed in an unsteady fluid flow. Although Wang et al.[13] derive a macroscopic momentum equation for moving porous media from the pore-scale microscopic equations by means of a volume-averaging approach, the motion of the porous body is achieved by a grid movement technique. One can also find approaches which simulate the dynamics of infinitely thin and porous boundaries. This is the case of the paper of [19] which makes use of IBM to simulate porous membranes by modelling the resistive behaviour of the membrane with a relative slip velocity in the normal direction between the boundary and the surrounding flow. The approach proposed by [20] is also based on IBM to simulate porous membranes and models the resistive force of the membrane by Darcy's law. Also taking advantage of the natural efficiency of the IBM in this context, [21] model in the same spirit the dynamics of a porous flapping filament by modelling the porosity in a similar way as [19], and point out the stabilizing effect of porosity on the wake, useful for flow control applications. These approaches are limited to infinitely thin boundaries and the porous effects are imposed by modelling the flux through the membrane, which is offering a given resistance to the flow.

In this work we also use the IBM approach, but the numerical framework we are proposing allows one to treat a volumetric porous medium, instead of simply the medium membrane, which is a significant improvement compared to existing approaches. Additionally, the porous model is not only restricted to modelling the flux through the membrane, but also includes the linear and non linear porous effects inside the volume medium.

The article is organized as follows. First, the numerical framework is presented by describing the LBM model for stationary and moving porous media, the IBM approach, and how the methods are coupled. Validation tests are then subsequently presented in steady configurations first, by doing a thorough comparison with existing literature results, and then on moving configurations to test the numerical framework in the case of immersed porous media with time-varying position.

ACCEPTED MANUSCRIPT

2. Numerical Methods

2.1. Lattice Boltzmann model for incompressible flows through stationary porous media

The generalised model proposed by Nithiarasu et al. [11] is used to simulate isothermal incompressible fluid flows through stationary porous media. In this approach, the flow is governed by the following generalised Navier-Stokes equations:

$$\frac{\partial \mathbf{u}}{\partial t} + (\mathbf{u} \cdot \nabla)\left(\frac{\mathbf{u}}{\varepsilon}\right) = -\frac{1}{\rho}\nabla(\varepsilon p) + \nu_\varepsilon \nabla^2 \mathbf{u} + \mathbf{F}, \tag{1}$$

satisfying the incompressibility condition $\nabla \cdot \mathbf{u} = 0$. In Eq.1, ρ is the fluid density, $\mathbf{u}$ and p are the volume-averaged velocity and pressure field, respectively, ν_ε is an effective kinematic viscosity, and $\mathbf{F}$ represents the total force field due to the presence of porous media and other external forces. This force term is given by:

$$\mathbf{F} = -\frac{\varepsilon \nu}{K}\mathbf{u} - \frac{\varepsilon F_\varepsilon}{\sqrt{K}}|\mathbf{u}|\mathbf{u} + \varepsilon \mathbf{G}, \tag{2}$$

where ν is the fluid kinematic viscosity, ε and K are the porosity and permeability of the porous medium, respectively, F_ε is its geometric function given by $F_\varepsilon = \frac{1.75}{\sqrt{150\varepsilon^3}}$, and $\mathbf{G}$ is an external force field. Note that the second term on the right side of Eq.1 is the Brinkman term, while the first and the second terms on the right side of Eq.2 are the linear (Darcy) and nonlinear (Forchheimer) drags due to the porous media, respectively. The dimensionless parameters that characterise the flow governed by Eq.1 are the Reynolds number, the porosity, the Darcy number, and the viscosity ratio, respectively defined by:

$$Re = \frac{LU}{\nu},\ \varepsilon = \frac{V_{void}}{V_{total}},\ Da = \frac{K}{L^2},\ J = \frac{\nu_\varepsilon}{\nu}, \tag{3}$$

where L is the characteristic length and U the velocity. In the following, the viscosity ratio is considered to be equal to 1.

In the LBM framework proposed by [12] to model an incompressible flow through a porous medium, the discretisation of the Lattice Boltzmann equation (LBE) takes the following form:

$$f_k(\mathbf{x} + \mathbf{e}_k \Delta t,\ t + \Delta t) - f_k(\mathbf{x},\ t) = -\frac{\Delta t}{\tau}\left(f_k(\mathbf{x},\ t) - f_k^{(eq)}(\mathbf{x},\ t)\right) + \Delta t F_k, \tag{4}$$

where $f_k(\mathbf{x},\ t)$ refers to the distribution functions (DF) at the position $\mathbf{x}$ and time t with particle velocity vector $\mathbf{e}_k$. The relaxation time τ is linked to the effective kinematic viscosity by $\nu_\varepsilon = c_s^2\left(\tau - \frac{1}{2}\right)\Delta t$. The equilibrium distribution function (EDF) is defined as:

$$f_k^{(eq)} = \omega_k \rho \left[1 + \frac{\mathbf{e}_k \cdot \mathbf{u}}{c_s^2} + \frac{\mathbf{u}\mathbf{u} : \left(\mathbf{e}_k \mathbf{e}_k - c_s^2 \mathbf{I}\right)}{2\varepsilon c_s^4}\right], \tag{5}$$

ACCEPTED MANUSCRIPT

where ω_k are the weight coefficients and c_s is the speed of sound. Both ω_k and c_s depend on the chosen lattice arrangement for the velocity discretisation. For the $D2Q9$ model, the discrete velocities are defined as follows:

$$\mathbf{e}_k = c \begin{pmatrix} 0 & 1 & -1 & 0 & 0 & 1 & -1 & -1 & 1 \\ 0 & 0 & 0 & 1 & -1 & 1 & 1 & -1 & -1 \end{pmatrix}, \; k = 0, 1, \ldots, 8, \tag{6}$$

where $c = \frac{\Delta x}{\Delta t}$ is the lattice speed, and Δx, Δt are the lattice spacing and the time step, respectively. In the current normalisation, the lattice speed is set to $c = 1$, $c_s = 1/\sqrt{3}$, and the weight coefficients are given by: $\omega_0 = 4/9$, $\omega_{1-4} = 1/9$, $\omega_{5-8} = 1/36$. Following [22], in order to match Eq.1, the discretised force term F_k takes the following form:

$$F_k = \omega_k \rho \left(1 - \frac{1}{2\tau}\right) \left[\frac{\mathbf{e}_k \cdot \mathbf{F}}{c_s^2} + \frac{\mathbf{u}\mathbf{F} : \left(\mathbf{e}_k \mathbf{e}_k - c_s^2 \mathbf{I}\right)}{\varepsilon c_s^4}\right]. \tag{7}$$

The macroscopic quantities (moments of the distribution function) are defined as:

$$\rho = \sum_k f_k, \tag{8a}$$

$$\rho \mathbf{u} = \sum_k \mathbf{e}_k f_k + \rho \frac{\Delta t}{2} \mathbf{F}, \tag{8b}$$

$$p = \frac{c_s^2 \rho}{\varepsilon}. \tag{8c}$$

Note that Eq.8b is a nonlinear equation for the velocity $\mathbf{u}$ as $\mathbf{F}$, given by Eq.2, also contains the velocity. However, as presented hereafter, the numerical developments will not be complicated by this issue because Eq.8b is quadratic, and thus, the velocity can be derived explicitly by:

$$\mathbf{u} = \frac{\mathbf{v}}{c_0 + \sqrt{c_0^2 + c_1 |\mathbf{v}|}}, \tag{9}$$

where $\mathbf{v}$ is a temporal velocity defined as:

$$\rho \mathbf{v} = \sum_k \mathbf{e}_k f_k + \frac{\Delta t}{2} \varepsilon \rho \mathbf{G}, \tag{10}$$

and the parameters c_0, c_1 are given by:

$$c_0 = \frac{1}{2}\left(1 + \varepsilon \frac{\Delta t}{2} \frac{\nu}{K}\right), \; c_1 = \varepsilon \frac{\Delta t}{2} \frac{F_\varepsilon}{\sqrt{K}}. \tag{11}$$

The obtention of Eq.9 to 11 follows the classical resolution of a quadratic equation, and is given in Appendix A.

ACCEPTED MANUSCRIPT

2.2. Lattice Boltzmann model for incompressible flows through moving porous media

For configurations involving moving porous structures, the unsteady effects of the porous media on the fluid are captured by the REV model proposed by [13], which consists in volume averaging the microscopic governing equations at the pore scale. As pointed out by [13], Galilean invariance can be obtained when using the intrinsic phase average velocity, and thus the macroscopic equations and the corresponding LBE model are only given in terms of the latter, which is defined as:

$$\langle \mathbf{u}_k \rangle^k = \frac{1}{V_k} \int_{V_k} \mathbf{u}_k dV, \tag{12}$$

where $k \in \{f, s\}$ with f and s denoting the fluid and solid phase, respectively. Thus, V_f is the volume occupied by the fluid phase in a representative volume V within the porous medium, and $V_s = V - V_f$ the volume occupied by the solid phase.

Consider a homogeneous and isotropic porous medium immersed in a Newtonian fluid. We assume that the medium moves with a rigid-body motion: $\mathbf{u}_s = \mathbf{U_p} + \mathbf{\Omega_p} \times \mathbf{r}$, where $\mathbf{U_p}$ and $\mathbf{\Omega_p}$ are the translational and rotational velocity, respectively, and $\mathbf{r}$ is the position vector measured from the body center. Note that $\mathbf{U_p}$ and $\mathbf{\Omega_p}$ remain unchanged even after taking the intrinsic phase average, and thus, for simplicity, $\langle \mathbf{u}_s \rangle^s$ will be denoted as $\mathbf{V_p}$ in the following. The flow is governed by the following macroscopic momentum equations:

$$\frac{\partial \langle \mathbf{u}_f \rangle^f}{\partial t} + \langle \mathbf{u}_f \rangle^f \cdot \nabla \langle \mathbf{u}_f \rangle^f = -\frac{1}{\rho_f} \nabla \langle p_f \rangle^f + \nu \nabla^2 \langle \mathbf{u}_f \rangle^f + \tilde{\mathbf{F}}, \tag{13}$$

satisfying the incompressibility condition $\nabla \cdot \langle \mathbf{u}_f \rangle^f = 0$. The total force field $\tilde{\mathbf{F}}$ in Eq.13 is given by:

$$\tilde{\mathbf{F}} = -\frac{\varepsilon \nu}{K} \left(\langle \mathbf{u}_f \rangle^f - \mathbf{V_p} \right) - \frac{\varepsilon^2 F_\varepsilon}{\sqrt{K}} |\langle \mathbf{u}_f \rangle^f - \mathbf{V_p}| \left(\langle \mathbf{u}_f \rangle^f - \mathbf{V_p} \right) + \tilde{\mathbf{G}}, \tag{14}$$

where $\tilde{\mathbf{G}}$ is an external force field.

The LBE is given by Eq.4, as in §2.1. However, following [13], the EDF and the discretised force term need to be modified as follows for the model to solve the volume-averaged equations for incompressible flows in moving porous media:

$$f_k^{(eq)} = \omega_k \rho \left[1 + \frac{\mathbf{e}_k \cdot \langle \mathbf{u}_f \rangle^f}{c_s^2} + \frac{\langle \mathbf{u}_f \rangle^f \langle \mathbf{u}_f \rangle^f : \left(\mathbf{e}_k \mathbf{e}_k - c_s^2 \mathbf{I} \right)}{2 c_s^4} \right], \tag{15}$$

and

$$F_k = \omega_k \rho \left(1 - \frac{1}{2\tau} \right) \left[\frac{\mathbf{e}_k \cdot \tilde{\mathbf{F}}}{c_s^2} + \frac{\langle \mathbf{u}_f \rangle^f \tilde{\mathbf{F}} : \left(\mathbf{e}_k \mathbf{e}_k - c_s^2 \mathbf{I} \right)}{c_s^4} \right]. \tag{16}$$

The macroscopic quantities are then obtained as follows:

$$\rho = \sum_k f_k, \tag{17a}$$

ACCEPTED MANUSCRIPT

$$\rho\langle\mathbf{u}_f\rangle^f = \sum_k \mathbf{e}_k f_k + \rho\frac{\Delta t}{2}\tilde{\mathbf{F}}, \tag{17b}$$

$$p = c_s^2\rho. \tag{17c}$$

As done previously in §2.1, an explicit formula for the velocity $\langle\mathbf{u}_f\rangle^f$ can be found by solving the quadratic nonlinear Eq.17b:

$$\langle\mathbf{u}_f\rangle^f = \frac{\langle\mathbf{v}_f\rangle^f}{d_0 + \sqrt{d_0^2 + d_1|\langle\mathbf{v}_f\rangle^f|}} + \mathbf{V_p}, \tag{18}$$

where $\langle\mathbf{v}_f\rangle^f$ is a temporal velocity defined as:

$$\rho\langle\mathbf{v}_f\rangle^f = \sum_k \mathbf{e}_k f_k - \rho\mathbf{V_p} + \frac{\Delta t}{2}\rho\tilde{\mathbf{G}}, \tag{19}$$

and d_0, d_1 are parameters given by:

$$d_0 = \frac{1}{2}\left(1 + \varepsilon\frac{\Delta t}{2}\frac{\nu}{K}\right),\ d_1 = \varepsilon^2\frac{\Delta t}{2}\frac{F_\varepsilon}{\sqrt{K}}. \tag{20}$$

2.3. Immersed Boundary method

The Immersed Boundary (IB) method is coupled to the LBE following the formulation presented in [18]. As in other variations of the IB method [14, 15, 23, 24, 25], a fixed Eulerian lattice is used for the flow field covering both the inside and outside of the immersed object, while a set of Lagrangian markers is used to track its boundary. However, in the present work, the basic idea is slightly different than the classical use of IB, as the force distributions $\mathbf{f}_{IB}$ which include the Darcy-Forchheimer porous force (Eq.2 or Eq.14) are computed on each Lagrangian marker to restore the desired velocity values in the immersed object at each time step. In particular, as can be seen in Fig.1, Lagrangian markers need to be placed also at the inside of it for its internal flow to be captured correctly.

As in classical IB methods, an interchange of information between the Eulerian lattices and the Lagrangian markers needs to be performed. To clarify notations, in the following lower case letters refer to variables evaluated on the Eulerian lattices, whilst upper case ones are used for the variables defined at the Lagrangian markers. Suppose that the velocity field $\mathbf{u}(\mathbf{x}, t)$ is known at time t. Let $\mathbf{X}_l(t + \Delta t)$ and $\mathbf{V}_{\mathbf{p},l}(t + \Delta t)$ $(l = 1, \ldots, N_l)$ be the desired position and velocity of the Lagrangian markers, respectively, to be obtained at time step completion. Then, the value of the velocity field interpolated at the l-th Lagrangian marker is given by the following discrete convolution:

$$\mathbf{U}_l = I[\mathbf{u}](\mathbf{X}_l) = \sum_{\mathbf{x}} \mathbf{u}(\mathbf{x}, t)\,\tilde{\delta}(\mathbf{x} - \mathbf{X}_l)\,(\Delta x)^d, \tag{21}$$

where $\sum_{\mathbf{x}}$ implies the summation over all the lattices $\mathbf{x}$, $\tilde{\delta}$ is a discretised Dirac's delta function, and d is the dimensionality of the problem. Note that the term

ACCEPTED MANUSCRIPT

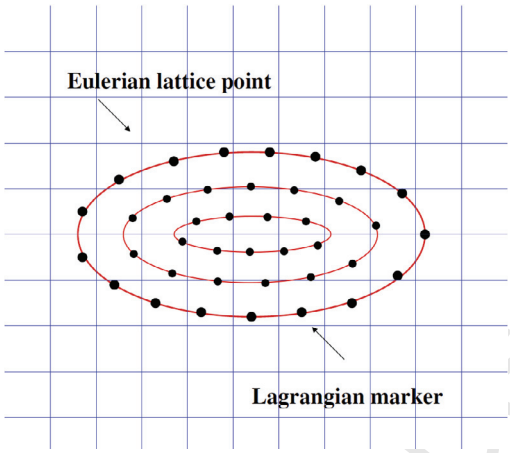

Figure 1: Schematic view of the Eulerian lattice points represented by the intersection points of the mesh lines and the Lagrangian markers denoted by the solid points used by the IB method for immersed porous objects.

$(\Delta x)^d$ is an Eulerian quadrature coming from the discrete approximation of an integral. Given $\mathbf{U}_l$, a system of singular forces $\mathbf{F}_{IB}(\mathbf{X}_l)$ can be defined on the Lagrangian markers. For a stationary porous object, $\mathbf{V}_{\mathbf{p},l}(t+\Delta t) = \mathbf{0}$ and the set of singular forces is given by Eq.2 as follows:

$$\mathbf{F}_{IB}(\mathbf{X}_l) = -\frac{\varepsilon\nu}{K}\mathbf{U}_l - \frac{\varepsilon F_\varepsilon}{\sqrt{K}}|\mathbf{U}_l|\mathbf{U}_l + \varepsilon\mathbf{G}_l. \tag{22}$$

Although the non-slip boundary condition is not explicitly enforced in the above equation, it will be shown later that the porous object behaves as a solid one for a low Darcy number, *i.e.* $Da \leq 10^{-6}$. For a moving porous object, $\mathbf{V}_{\mathbf{p},l}(t+\Delta t)$ is found by solving the motion equations, and the system of singular forces is given by Eq.14 as:

$$\mathbf{F}_{IB}(\mathbf{X}_l) = -\frac{\varepsilon\nu}{K}(\mathbf{U}_l - \mathbf{V}_{\mathbf{p},l}) - \frac{\varepsilon^2 F_\varepsilon}{\sqrt{K}}|\mathbf{U}_l - \mathbf{V}_{\mathbf{p},l}|(\mathbf{U}_l - \mathbf{V}_{\mathbf{p},l}) + \tilde{\mathbf{G}}_l. \tag{23}$$

Finally, the singular forces $\mathbf{F}_{IB}(\mathbf{X}_l)$ are spread onto the neighboring lattices using the following formula:

$$\mathbf{f}_{IB} = S[\mathbf{F}_{IB}](\mathbf{x}) = \sum_{l=1}^{N_l} \mathbf{F}_{IB}(\mathbf{X}_l)\,\tilde{\delta}(\mathbf{x}-\mathbf{X}_l)\,\epsilon_l, \tag{24}$$

where ϵ_l is a Lagrangian quadrature determined so as to enforce the reversibility of the interpolation and spreading operations. It is found by solving the linear system:

$$A\overrightarrow{\epsilon} = \overrightarrow{1}, \tag{25}$$

ACCEPTED MANUSCRIPT

with $A = \{\alpha_{k,l}\}_{k,l=1,..,N_l} = \sum_{\mathbf{x}} \tilde{\delta}\left(\mathbf{x} - \mathbf{X}_l\right) \tilde{\delta}\left(\mathbf{x} - \mathbf{X}_k\right) (\Delta x)^d$ and $\overrightarrow{1} = (1, 1, \ldots, 1)^T$. More details can be found in [18, 26].

Here, the discretised Dirac's delta $\tilde{\delta}$ proposed by Roma et al.[27] has been chosen to perform the convolution in Eqs.21 and 24:

$$\tilde{\delta}(r) = \begin{cases} \frac{1}{6}\left(5 - 3|r| - \sqrt{-3\left(1 - |r|\right)^2 + 1}\right) & , \ 0.5 \leq |r| \leq 1.5, \\ \frac{1}{3}\left(1 + \sqrt{-3r^2 + 1}\right) & , \ |r| \leq 0.5, \\ 0 & , \ 1.5 \leq |r|. \end{cases} \tag{26}$$

If r is a vector, then the multidimensional discretised Dirac's delta is simply given by: $\tilde{\delta}(x, y, z) = \frac{1}{\Delta x^3} \tilde{\delta}\left(\frac{x}{\Delta x}\right) \cdot \tilde{\delta}\left(\frac{y}{\Delta x}\right) \cdot \tilde{\delta}\left(\frac{z}{\Delta x}\right)$. For more details, the reader is referred to [26].

2.4. Algorithm of computation

The computational procedure of the proposed IB-LBM framework for simulating the coupled dynamics between a moving [or stationary] porous object and a surrounding fluid can be summarized as follows:

Step 0 Set the initial values of the density and velocity field at time $t = 0$, $\rho(\mathbf{x}, t = 0)$ and $\langle \mathbf{u}_f \rangle^f (\mathbf{x}, t = 0)$ $[\mathbf{u}(\mathbf{x}, t = 0)]$, and compute the EDF, $f_k^{(eq)}(\mathbf{x}, t = 0)$, using Eq.15 [Eq.5]. Assign $f_k(\mathbf{x}, t = 0) = f_k^{(eq)}(\mathbf{x}, t = 0)$.

Step 1 Compute the desired position and velocity of the Lagrangian markers, $\mathbf{X}_l(t + \Delta t)$ and $\mathbf{V}_{\mathbf{p},l}(t + \Delta t)$, to be obtained at time step completion, by solving the motion equations. The matrices related to the porous structure, namely ε and Da, as well as $\tilde{\delta}$ and ϵ_l need to be updated due to the position change of the Lagrangian markers. [For a stationary porous object, this step is neglected.]

Step 2 Obtain the velocity field $\mathbf{U}_l$ at the l-th Lagrangian marker by Eq.21.

Step 3 Compute the Lagrangian forcing, $\mathbf{F}_{IB}(\mathbf{X}_l)$, required to enforce the desired Darcy-Forchheimer drags due to the presence of the porous object, and impose the desired velocity condition at each Lagrangian marker, for a kinematic compatibility to be provided between the porous and the fluid motion, using Eq.23 [Eq.22].

Step 4 Spread the Lagrangian forcing onto the lattice neighbours using Eq.24.

Step 5 Obtain the density and velocity field at the next time step, $\rho(\mathbf{x}, t + \Delta t)$ and $\langle \mathbf{u}_f \rangle^f (\mathbf{x}, t + \Delta t)$ $[\mathbf{u}(\mathbf{x}, t + \Delta t)]$, by solving the LBEq. 4. The solution process of the LBE can be outlined below:

1. Discretise the Eulerian forcing, $\mathbf{f}_{IB}$, obtained by Step 4 on the lattice discrete directions using Eq.16 [Eq.7]. Perform the collision process:

$$f_k^*(\mathbf{x}, t) = f_k(\mathbf{x}, \ t)(1 - \omega\Delta t) + \omega\Delta t f_k^{(eq)}(\mathbf{x}, \ t) + \Delta t F_k,$$

where $\omega = \frac{1}{\tau}$ is the relaxation frequency.

ACCEPTED MANUSCRIPT

2. Perform the streaming: $f_k\left(\mathbf{x}+\mathbf{e}_k\Delta t, t+\Delta t\right) = f_k^*\left(\mathbf{x}, t\right)$.
3. Modify the DF, f_k, at the boundaries of the computational domain to satisfy the desired boundary conditions.
4. Calculate the macroscopic quantities at the next time step $t+\Delta t$ using Eqs.17a-20 [Eqs.8a-11].
5. Calculate the EDF at the next time step, $f_k^{(eq)}\left(\mathbf{x}, t+\Delta t\right)$, using Eq.15 [Eq.5].

Step 6 Repeat the Steps 1-5 until a desired convergence criterion is satisfied.

3. Numerical Validation

To validate the proposed numerical method, a three-step process is performed. First, a static configuration of a circular porous cylinder in cross flow is considered for different Reynolds numbers in §3.1. Although this kind of configuration can be tackled without the use of IB, it allows to assess in detail the ability of the method to capture both integral and local quantities, by comparing with existing literature studies on a detailed and clearly defined flow topology. In a second step, a more complex configuration is examined in §3.2, where the proposed algorithm is needed to capture both porosity and motion of the geometry in a steady flow. It consists of a porous circular cylinder positioned at the middle of the channel. The problem is solved in two frames of reference, out of which the first one is fixed on the cylinder, while the second one is fixed on the channel walls. This configuration allows us to validate the proposed coupled method in the case of a moving porous body, showing alongside the Galilean invariance of the macroscopic equations derived in terms of the intrinsic phase average velocity. Finally, a cylinder undergoing forced oscillations in cross flow is examined in the rigid case (§3.3) to compare with existing literature results. Through this test case, we can demonstrate a good agreement with reference results for unsteady flows, and particularly in the crucial case of a locked-in configuration.

3.1. Flow around and through a stationary porous circular cylinder in steady flow

The flow around and through a stationary porous circular cylinder at low Reynolds numbers (based on the free-stream velocity U_∞ and the cylinder diameter D) is chosen to validate the proposed method. The cylinder is placed at the center of a computational domain of dimensions $60D \times 60D$. A uniform velocity U_∞ is assigned at the inlet plane [28], while a convective boundary condition is implemented at the far field boundaries [29]. The flow is considered to be converged to a steady-state if the relative L_2 error norm of the velocity field, namely $\frac{\|\mathbf{u}(\mathbf{x},t+\Delta t)-\mathbf{u}(\mathbf{x},t)\|_2}{\|\mathbf{u}(\mathbf{x},t+\Delta t)\|_2}$, is less than or equal to 10^{-6}. At this steady-state, a recirculation bubble may be formed either at the rear side of the cylinder, or inside of it. The wake parameters measured here are: the wake length L_f

ACCEPTED MANUSCRIPT

normalised by D, and the separation angle θ_s from the rear stagnation point of the cylinder. The drag coefficient, defined by $C_D = \frac{2F_D}{\rho U_\infty^2 D}$ (where F_D is the drag force), is another important flow parameter to be computed.

The present simulations were performed using both the model of Guo & Zhao (discussed in §2.1) as well as the algorithm proposed in §2.4. The fluid density is taken as $\rho = 1$, while the relaxation time is set to be $\tau = 0.65$. The Reynolds number varies between 10 and 40 with a Darcy number equal to $2.5 \cdot 10^{-3}$ or $2.5 \cdot 10^{-4}$ in the porous region. The porosity is chosen such that the Carman-Kozeny equation is satisfied, $K = \frac{\varepsilon^3 d_p^2}{180(1-\varepsilon)^2}$ (where d_p is the characteristic diameter of a particle in the porous aggregate, taken the value of 100μm here as in [3]), resulting in the corresponding values $\varepsilon = 0.993$ or $\varepsilon = 0.977$. In the fluid region, the porosity is set equal to 1 and a value of 10^7 is assigned for the Da, as in the work of Nithiarasu et al.[11]. Note that the drag force is computed by the momentum exchange method for the model of Guo & Zhao. Although F_D is usually calculated from the summation of the forces at the Lagrangian markers in the IB methods, it was found that this approach could not provide a correct estimation of the drag in the case of the present porous configuration. For that reason, the control volume method is preferred to compute the force coefficients. Both methods mentioned here for the drag calculation are briefly reviewed in Appendix B.

To ensure a grid-independent solution, a study was performed with three different mesh sizes at $Re = 20$ and $Da = 2.5 \cdot 10^{-3}$ ($\varepsilon = 0.993$). The comparison of the drag coefficient, the wake length and the separation angle at the various mesh sizes is shown in Table 1. For the results obtained by the model of Guo & Zhao, the differences in the aforementioned variables between the two meshes of 1201×1201 and 2401×2401 are all less than 1.5%, indicating that the mesh of 1201×1201 is fine enough. However, the solutions obtained by our algorithm are more sensitive to the mesh size. Although the difference in the drag coefficient and the separation angle between the second and the third case is less than 1.5% and 2.5%, the corresponding difference in the wake length is of 6.2%. Therefore, the mesh of the third case is chosen for the following simulations.

In order to examine the accuracy of the present method, simulations were performed for different Reynolds numbers and $Da = 2.5 \cdot 10^{-3}$ or $2.5 \cdot 10^{-4}$,

Case	**Mesh Size**	**References**	$\mathbf{C_d}$	$\mathbf{L_f}$	$\theta_\mathbf{s}$
$D = 10$	601×601	Guo & Zhao model	2.028	0.800	28.6°
		Present method	2.106	0.940	31.6°
$D = 20$	1201×1201	Guo & Zhao model	1.934	0.700	27.9°
		Present method	2.017	0.770	29.3°
$D = 40$	2401×2401	Guo & Zhao model	1.909	0.700	27.7°
		Present method	1.989	0.725	28.6°

Table 1: Effect of mesh size on the drag coefficient, the wake length and the separation angle at $Re = 20$ and $Da = 2.5 \cdot 10^{-3}$ ($\varepsilon = 0.993$).

ACCEPTED MANUSCRIPT

Case	References	C_d	L_f	θ_s
$Re = 10$	Guo & Zhao model	2.668	-	-
	Present method	2.781	-	-
	Yu et al.[30]	2.531	-	-
	Bhattacharyya et al.[3]	2.767	-	-
$Re = 20$	Guo & Zhao model	1.909	0.700	27.7°
	Present method	1.989	0.725	28.6°
	Yu et al.[30]	1.870	-	-
	Bhattacharyya et al.[3]	2.007	0.700	29.0°
$Re = 30$	Guo & Zhao model	1.632	1.330	32.6°
	Present method	1.694	1.390	33.2°
	Yu et al.[30]	1.610	-	-
	Bhattacharyya et al.[3]	1.716	1.400	34.0°
$Re = 40$	Guo & Zhao model	1.489	2.030	33.5°
	Present method	1.570	2.103	33.9°
	Yu et al.[30]	1.464	-	-
	Bhattacharyya et al.[3]	1.557	2.000	37.0°

Table 2: Comparison of the drag coefficient, the wake length and the separation angle at different Reynolds numbers and $Da = 2.5 \cdot 10^{-3}$ ($\varepsilon = 0.993$).

Case	References	C_d	L_f	θ_s
$Re = 10$	Guo & Zhao model	2.802	0.230	29.6°
	Present method	2.919	0.250	29.6°
	Bhattacharyya et al.[3]	2.904	0.200	24.0°
$Re = 20$	Guo & Zhao model	1.976	0.850	41.0°
	Present method	1.991	0.890	41.9°
	Bhattacharyya et al.[3]	2.021	0.875	38.0°
$Re = 30$	Guo & Zhao model	1.646	1.480	46.1°
	Present method	1.783	1.550	47.2°
	Bhattacharyya et al.[3]	1.811	1.550	44.0°
$Re = 40$	Guo & Zhao model	1.474	2.150	49.0°
	Present method	1.619	2.230	50.0°
	Bhattacharyya et al.[3]	1.602	2.200	48.0°

Table 3: Comparison of the drag coefficient, the wake length and the separation angle at different Reynolds numbers and $Da = 2.5 \cdot 10^{-4}$ ($\varepsilon = 0.977$).

and the results were compared with the numerical ones of Bhattacharyya et al.[3] and Yu et al.[30]. Tables 2 and 3 compare in detail the methods on the computation of an integrated quantity which is classically used in literature to assess the validity of numerical methods, the drag coefficient, as well as two local quantities characterising the topology of the flow, the wake length and the separation angle.

ACCEPTED MANUSCRIPT

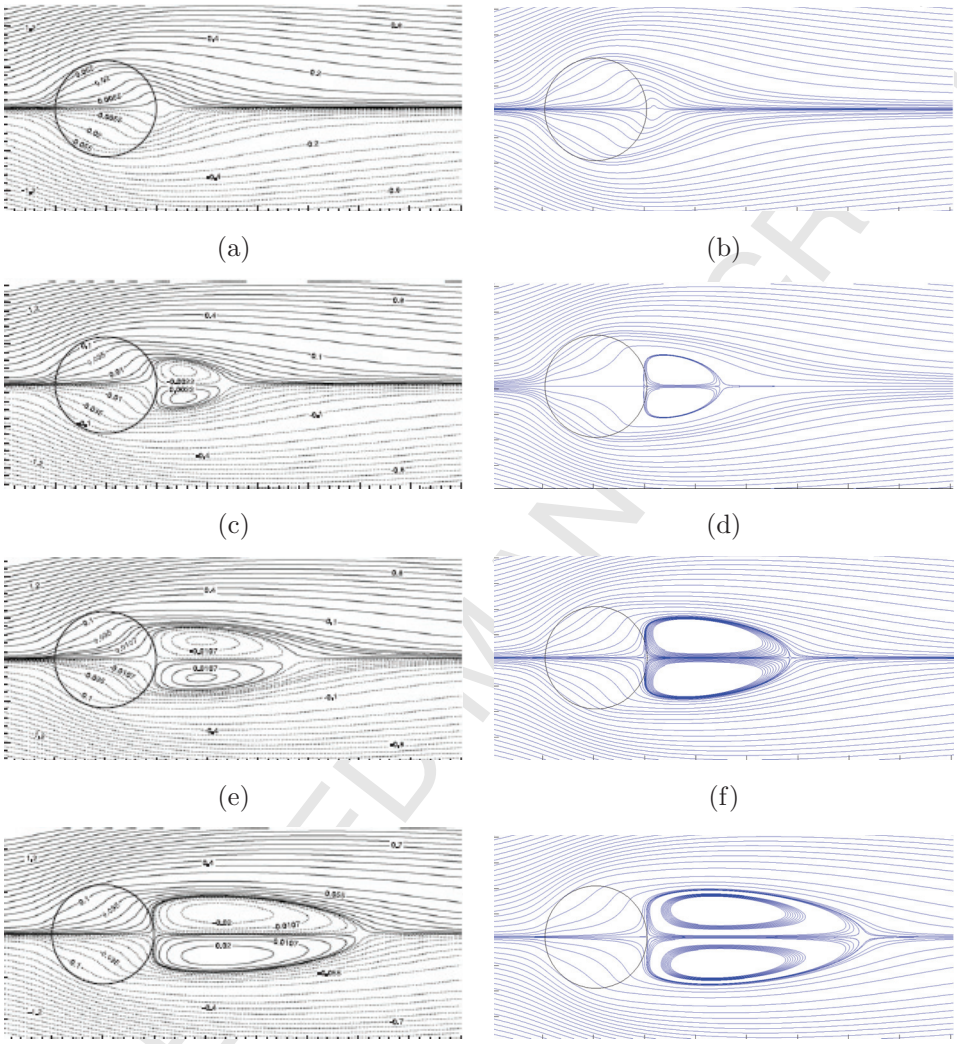

Figure 2: Streamlines of the flow through the porous cylinder at $Da = 2.5 \cdot 10^{-3}$ ($\varepsilon = 0.993$) and (a-b) $Re = 10$, (c-d) $Re = 20$, (e-f) $Re = 30$, (g-h) $Re = 40$. The figures on the left column have been obtained by Bhattacharyya et al.[3], while the right column ones are the results obtained with the proposed method.

The overall agreement is excellent. The average relative error in the drag coefficient between the results of our algorithm and the ones of Bhattacharyya et al.[3] is around 1%, while the corresponding error rises up to 5% for the results obtained by the model of Guo & Zhao. In general, the wake length found by our method lies closer to the reference length than the one predicted by Guo & Zhao's model. The relative error is in average around 2%, apart from the first

ACCEPTED MANUSCRIPT

case of Table 3. A significant declination in the separation angle can also be observed for this case, while the average relative difference in θ_s is up to 6%. The body-fitted mesh used in the work of Bhattacharyya et al.[3] could be a possible explanation for this discrepancy, as the flow field close to the cylinder surface can be better captured by such a mesh. Finally, the streamlines for $Da = 2.5 \cdot 10^{-3}$ are presented in Fig.2. The very good agreement is confirmed by looking at the close similarities in both the internal and external flow fields. In particular, the formation of the small and symmetrical recirculation bubble at the rear side of the cylinder at $Re = 10$ is properly captured (Fig.2 a-b). The comparisons provided on the subsequent subfigures of Fig.2 clearly show that the thickness and length of the external recirculation bubble is similar to [3], while the internal flow through the cylinder, and at its rear part of the cylinder is correctly captured by the proposed method.

3.2. Flow past a porous circular cylinder inside a channel

In this section, the flow past a porous circular cylinder inside a channel is investigated. Following the methodology of Wang et al. [13], the simulations are performed in two frames of reference. In the first case, denoted by $R1$, the channel walls move with a constant horizontal velocity U, while the cylinder is fixed at the centerline of the domain. In the case $R2$, the walls of the channel are fixed, whilst the cylinder is moving along the channel centerline with a constant horizontal velocity $-U$. Since the macroscopic equations with the intrinsic phase average velocity are employed in the current work, the Galilean invariance of the $R1$ and $R2$ frames is ensured, meaning that the relative motion between the channel flow and the porous cylinder is identical in the two frames.

As in the work of Wang et al. [13], the cylinder of diameter $D = 24$ is initially located at the middle of the computational domain. The channel of dimensions $L \times H = 15D \times 15D$ is covered by a 360×359 uniform mesh. Periodic boundary conditions are considered at the channel inlet and outlet for both frames of reference. In the $R1$ frame, the Zou & He known velocity boundary conditions [28] are implemented at the channel walls, while a half-way bounce-back scheme is applied on them in the $R2$ case. In the latter case, the motion of the cylinder is accomplished by the proposed algorithm considering that $\mathbf{V}_{\mathbf{p},l}(t + \Delta t) = (-U, 0)$. Two simulations are performed here; the first one is for $\varepsilon = 0.7$ and $Da = 10^{-3}$, while the second one corresponds to $\varepsilon = 0.3$ and $Da = 10^{-4}$. The Reynolds number, defined as: $Re = \frac{UD}{\nu}$, is set to the value of 1 for all the simulations.

In Fig. 3 and 4, the profiles of the intrinsic phase average velocity through the channel vertical centerline (Fig. 3, 4(a)) and along the horizontal lines at $y/H = 0.4708$ (Fig. 3, 4(b)) and $y/H = 0.4986$ (Fig. 3, 4(c)) as well as the drag force F_x against the dimensionless time $\frac{tU}{L}$ (Fig. 3, 4(d)) are presented. As it can be seen from the figures, an excellent agreement is obtained for the results between the two reference frames for both the simulations. The results in the $R1$ and $R2$ frames are perfectly superimposed, demonstrating the aforementioned Galilean invariance of the macroscopic equations. Also, the present results are in excellent agreement with the ones of Wang et al. [13].

ACCEPTED MANUSCRIPT

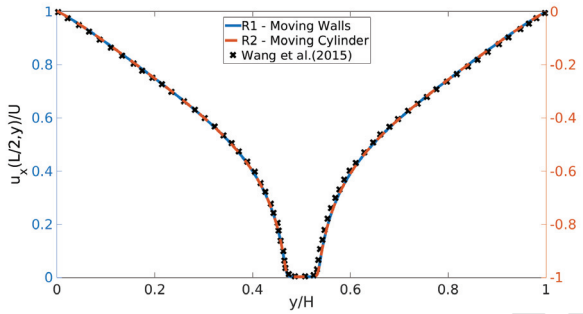

(a)

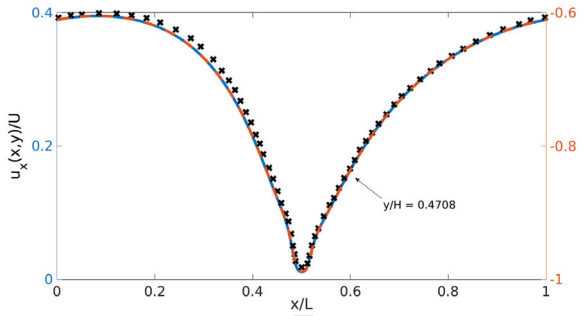

(b)

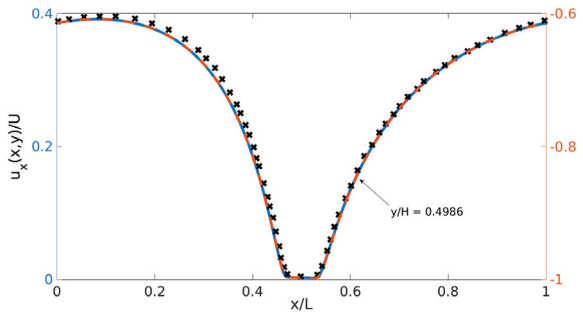

(c)

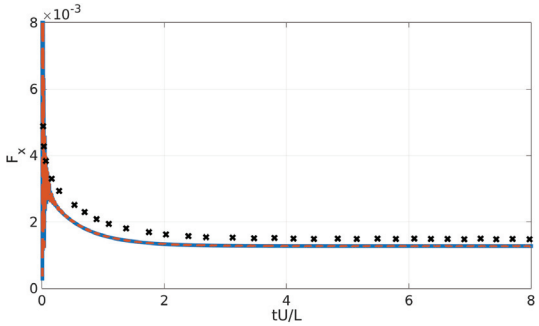

(d)

Figure 3: Velocity profiles and the drag force for $\varepsilon = 0.7$ and $Da = 10^{-3}$.

ACCEPTED MANUSCRIPT

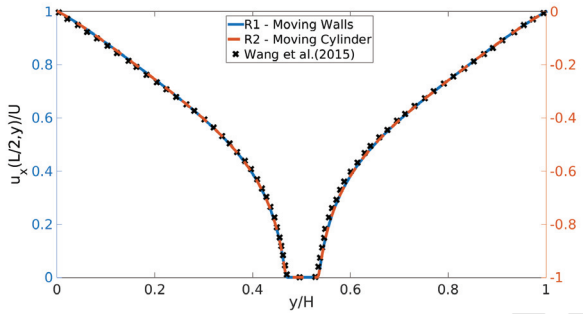

(a)

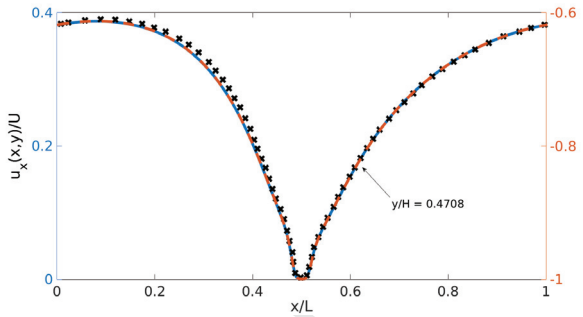

(b)

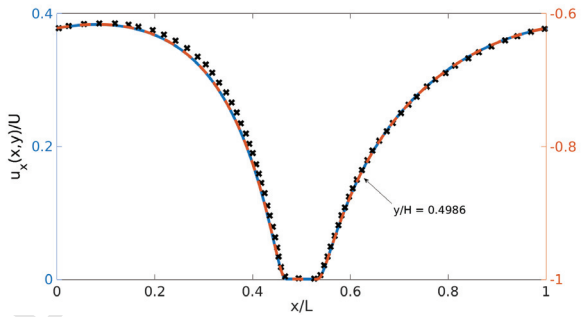

(c)

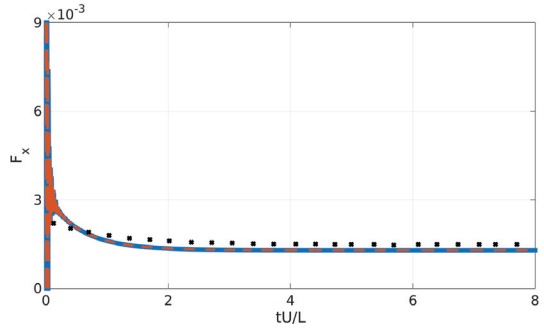

(d)

Figure 4: Velocity profiles and the drag force for $\varepsilon = 0.3$ and $Da = 10^{-4}$.

ACCEPTED MANUSCRIPT

3.3. Flow around and through a porous circular cylinder with forced cross-flow oscillations

To further validate the method, the configuration of a porous circular cylinder undergoing forced cross-flow oscillations in an unsteady flow is studied. The challenge here is two-fold: a first difficulty is the implementation of the motion of a porous immersed object in unsteady flow, and on the other hand there is a lack of literature studies for such a porous configuration. However, a similar configuration has been extensively studied both numerically and experimentally in the case of a rigid cylinder [31, 32, 33, 34, 35, 36, 37]. For this reason, we choose to simulate the flow around an unsteady solid cylinder by assigning a low value for the porosity and Darcy number inside the cylinder, namely $\varepsilon = 0.1$ and $Da = 10^{-6}$.

A computational domain of dimensions $46.5D \times 22D$, where D is the cylinder diameter, is considered. The center of the cylinder is initially placed at $(12.5D, 11D)$. The free-stream velocity U_∞ is considered at the inflow, while a convective boundary condition is applied at the outflow. A Neumann boundary condition is implemented at the top and bottom boundary. The motion of the cylinder is governed by the following equations:

$$\begin{aligned} x &= \text{constant} \\ y\left(t\right) &= Y_{\max} \sin\left(2\pi F_0 t\right), \end{aligned} \tag{27}$$

where $Y_{\max}$ and F_0 are the amplitude and the frequency of the oscillation. The dimensionless parameters are the Reynolds number, defined as: $Re = \frac{U_\infty D}{\nu}$, the adimensional amplitude $A = Y_{\max}/D$ and the frequency ratio $F = F_0/F_s$, where F_s is the natural frequency of the flow around the stationary cylinder.

Resulting from the coupling between the forced oscillations of the cylinder and the flow structure, the so-called lock-in phenomenon occurs here, when the vortex shedding frequency synchronizes to the natural vibration frequency of the cylinder. Two simulations are performed with the present algorithm for $A = 0.2$, and the results are compared to those of Nobari & Naderan [36]. The first simulation at $F = 0.6$ corresponds to an unlocked case, while the second at $F = 1.05$ recovers a locked one.

As the grid dependence on this unsteady configuration is particularly important, a grid-sensitivity analysis is initially performed for the stationary cylinder case. Table 4 shows the comparison of the mean drag coefficient $\left(\overline{C_D}\right)$, the

Case	$\mathbf{\overline{C_D}}$	$\mathbf{C'_D}$	$\mathbf{C'_L}$	**St**
$D = 20$	1.513	± 0.015	± 0.367	0.159
$D = 40$	1.414	± 0.011	± 0.356	0.164
$D = 80$	1.375	± 0.010	± 0.336	0.166

Table 4: Effect of the grid size on the aerodynamic coefficients and the Strouhal number at $Re = 100$ and $Da = 10^{-6}$ $(\varepsilon = 0.1)$.

ACCEPTED MANUSCRIPT

References	$\overline{C_D}$	C'_D	C'_L	St
Present method ($D = 40$)	1.414	$\pm$0.011	$\pm$0.356	0.164
Williamson [32] (exp.)	-	-	-	0.166
Lai & Peskin [38]	1.447	-	$\pm$0.330	0.165
Uhlmann [34]	1.453	$\pm$0.011	$\pm$0.339	0.169
Wu & Shu [15]	1.364	-	$\pm$0.344	0.163
Nobari & Naderan [36]	1.720	-	-	0.170

Table 5: Comparison of the aerodynamic coefficients and the Strouhal number for the flow around a stationary cylinder at $Re = 100$.

amplitude of the drag (C'_D) and lift (C'_L) fluctuations and the Strouhal number (St) obtained on three different grids. Although the relative errors in the mean drag coefficient and the Strouhal number between the grids of the second and third case are both less than 3%, the difference in the amplitude of the lift fluctuations is up to 6%. However, we choose to use the second grid ($D = 40$) to reduce the computational cost, while keeping a reasonable margin of error. The results for this grid are compared to literature ones in Table 5. Both the mean drag coefficient and the Strouhal number are within the range of the reference results, while the amplitude of the drag fluctuations is in excellent agreement with the one of Uhlmann [34]. The maximal lift coefficient is quite over-predicted, but the percentage difference from the work of Wu & Shu [15], where the flow is also solved by an IB-LB method, is less than 3.5%.

The time histories of the drag and lift coefficient for the oscillating cylinder at $Re = 100$, $A = 0.2$ and $F = 0.6$ or $F = 1.05$ are presented in Figs.5 and 6. When the lock-in phenomenon occurs, the coupled system is dominated by a single frequency, and thus the time evolution of the aerodynamic coefficients is characterised by a pure sinusoidal response, as in Figs.5(b) and 6(c-d). In the case where lock-in does not happen, the aerodynamic coefficients do not exhibit any longer a sinusoidal form, but a more complex beating behaviour is observed, resulting from the presence of multiple frequencies in the flow. As it

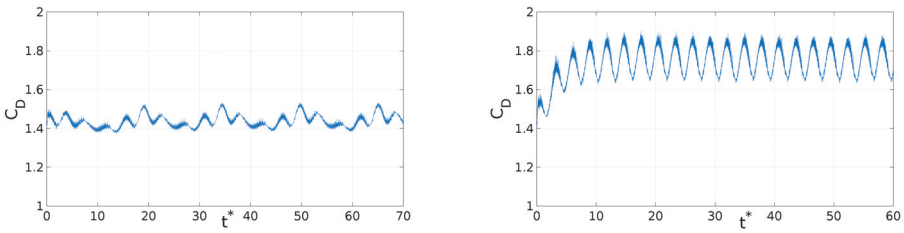

Figure 5: Variation of the drag coefficient versus the adimensional time $t^* = \frac{tU_\infty}{D}$ at (a) $F = 0.6$ and (b) $F = 1.05$.

ACCEPTED MANUSCRIPT

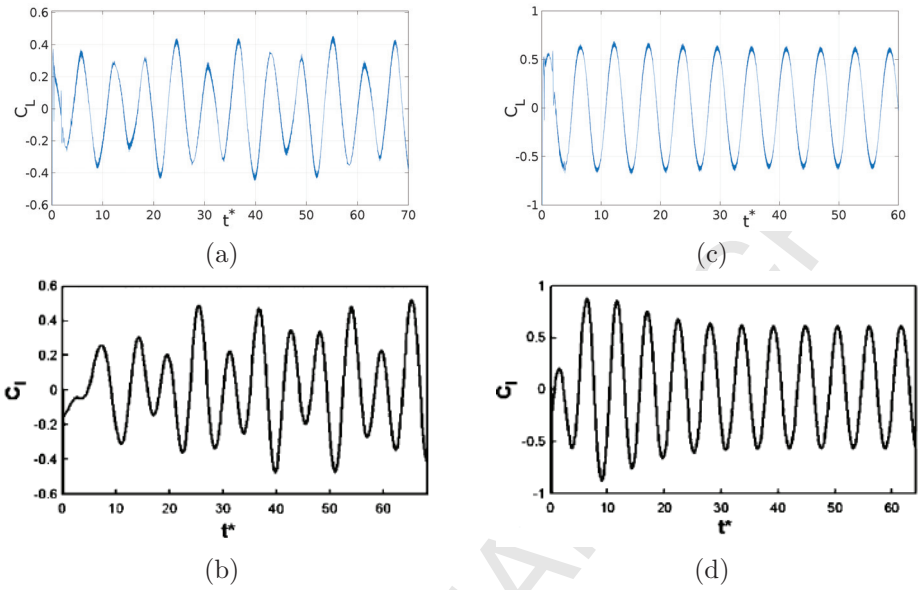

Figure 6: Variation of the lift coefficient versus the adimensional time t^* at (a-b) $F = 0.6$ and (c-d) $F = 1.05$. The figures (b) and (d) were obtained by Nobari & Naderan [36].

can be seen in Figs.5(a) and 6(a-b), the drag and lift signals are not periodic over two successive oscillation cycles, but rather over several ones.

Globally, the current results agree well with the ones of Nobari & Naderan [36]. The mean drag coefficients found here are 1.44 and 1.75 for $F = 0.6$ and $F = 1.05$ respectively, while the reference ones are 1.72 and 2.00. These relatively high differences with [36] are balanced by the fact that the reference mean drag coefficient is over-predicted compared to the other numerical results even in the case of the stationary cylinder, $\overline{C_{D,ref}} = 1.720$ (see Table 5). Regarding the lift coefficient, both the amplitude and the peaks for the unlocked case are well captured. The amplitude of the highest peak in Fig.6(a) is found to be 0.44 which agrees well with the reference one of 0.49. A value of $C'_L = \pm 0.61$ is found for the locked configuration, which is in excellent agreement with the reference one, $C'_{L,ref} = \pm 0.61$.

4. Conclusions

A new algorithm based on the Lattice Boltzmann and Immersed Boundary methods for incompressible flows through stationary or moving porous media has been proposed. Contrary to previous works where a stair-case approximation or a body-fitted mesh are used to represent curved porous objects, the immersed porous surface can now be described smoothly by the Lagrangian markers regardless of its geometry, while the flow is still solved on a Cartesian

ACCEPTED MANUSCRIPT

mesh. This approach allows one to tackle easily the fluid-structure interaction of moving porous bodies, while avoiding a costly grid movement technique.

The method has initially been applied to the steady flow through a stationary porous circular cylinder for different Reynolds and Darcy numbers. An excellent agreement has been obtained for the wake parameters and the drag coefficient, while the flow field has also been properly captured both internally and externally. The steady flow past a porous circular cylinder inside a channel has then been considered so as to validate the method in the case of a moving porous object. The simulations were performed in two frames of reference, and their results presented a perfect agreement with each other as well as with the reference ones. The forced cross-flow oscillations of a porous circular cylinder have finally been examined for validating the proposed algorithm in the case of a moving porous object in unsteady flow. The aerodynamic coefficients have demonstrated a good agreement with the reference results for both a locked and an unlocked configuration.

The present approach constitutes a stepping-stone for the numerical simulation of moving porous media for flow control applications. In particular, poroelastic coatings around bluff bodies will be considered in the future for separation control and increased aerodynamic performance purposes. The proposed algorithm will also be extended for simulating volumetric porous membranes undergoing deformation.

Appendix A. Derivation of the explicit formula of the velocity field (Eq.9-11) from the quadratic nonlinear Eq.8b (based on [12])

By substituting Eq.2 to Eq.8b, one can find that:

$$\rho\mathbf{u} = \sum_k \mathbf{e_k} f_k + \rho\frac{\Delta t}{2}\left(-\frac{\varepsilon\nu}{K}\mathbf{u} - \frac{\varepsilon F_\varepsilon}{\sqrt{K}}|\mathbf{u}|\mathbf{u} + \varepsilon\mathbf{G}\right) \Rightarrow$$

$$\rho\frac{\Delta t}{2}\frac{\varepsilon F_\varepsilon}{\sqrt{K}}|\mathbf{u}|\mathbf{u} + \rho\left(1 + \frac{\Delta t}{2}\frac{\varepsilon\nu}{K}\right)\mathbf{u} - \left(\sum_k \mathbf{e_k} f_k + \rho\frac{\Delta t}{2}\varepsilon\mathbf{G}\right) = 0,$$

where the DF f_k, the density ρ, the velocity field $\mathbf{u}$ and the external force field $\mathbf{G}$ are all determined at position $\mathbf{x}$ and time t. Defining the temporal velocity field $\mathbf{v}$ and the parameters c_0, c_1 as in Eqs.10 and 11, the above equation takes the following form:

$$\rho c_1|\mathbf{u}|\mathbf{u} + 2\rho c_0\mathbf{u} - \rho\mathbf{v} = 0.$$

Since $\rho \neq 0$, it should hold that:

$$c_1|\mathbf{u}|\mathbf{u} + 2c_0\mathbf{u} - \mathbf{v} = 0 \Rightarrow$$

$$\mathbf{u} = \frac{\mathbf{v}}{c_1|\mathbf{u}| + 2c_0}.$$

ACCEPTED MANUSCRIPT

Notice that the denominator is a scalar. Taking the norm of the above condition, we get a quadratic equation with respect to $|\mathbf{u}|$:

$$|\mathbf{u}| = \frac{|\mathbf{v}|}{c_1|\mathbf{u}| + 2c_0} \Rightarrow$$

$$c_1|\mathbf{u}|^2 + 2c_0|\mathbf{u}| - |\mathbf{v}| = 0,$$

whose roots are:

$$-\frac{1}{c_1}\left(c_0 + \sqrt{c_0^2 + c_1|\mathbf{v}|}\right) \text{ and } -\frac{1}{c_1}\left(c_0 - \sqrt{c_0^2 + c_1|\mathbf{v}|}\right).$$

Only the second root is accepted, as the first one would require the norm of the velocity field $|\mathbf{u}|$ to get a negative value. By substituting the accepted formula for $|\mathbf{u}|$ to the aforementioned condition, we conclude to the desired Eq.9.

Appendix B. Calculation of the Aerodynamic Forces

Appendix B.1. Momentum Exchange Method

Consider the scalar array $w(i,j)$ at which is assigned a value of 0 if the lattice (i,j) is occupied by fluid, or a value of 1 if the lattice (i,j) is inside the porous body. The momentum exchange (per unit time) in the k-th lattice direction and its opposite one $\bar{k}$ between the porous boundary lattice $\mathbf{x_b}$ and the neighboring fluid node $\mathbf{x_n} = \mathbf{x_b} + \mathbf{e_{\bar{k}}}\Delta t$ at time t is:

$$\frac{1}{\Delta t}\left(\mathbf{e_k} f_k(\mathbf{x_b}, t) - \mathbf{e_{\bar{k}}} f_{\bar{k}}(\mathbf{x_n}, t)\right),$$

where $\mathbf{e_{\bar{k}}} = -\mathbf{e_k}$ denotes the particle velocity vector in the opposite of the k-th direction. Summing the contribution of the momentum exchange with all possible neighboring fluid-state lattices over all the porous boundary nodes $\mathbf{x_b}$, the total force $\mathbf{F} = (F_D, F_L)$ exerted on the fluid by the porous body is found to be:

$$\mathbf{F} = \sum_{\mathbf{x_b}} \sum_{k \neq 0} \mathbf{e_k}\left(f_k(\mathbf{x_b}, t) + f_{\bar{k}}(\mathbf{x_b} + \mathbf{e_{\bar{k}}}\Delta t, t)\right)\left(1 - w(\mathbf{x_b} + \mathbf{e_{\bar{k}}}\Delta t)\right)\frac{\Delta x^2}{\Delta t}.$$

Further details can be found in the work of Mei et al.[39].

Appendix B.2. Control Volume Method

Let Ω be a flow domain bounded by the surface S which contains a stationary solid body of volume Ω_b. The total force acting on the fluid by the rigid body is:

$$\mathbf{F_{stat}} = -\frac{\partial}{\partial t}\int_\Omega \rho \mathbf{u} dV - \oint_S \rho \mathbf{u}(\mathbf{u} \cdot \mathbf{dS}) - \oint_S p \cdot \mathbf{dS} + \oint_S \bar{\bar{\tau}} \cdot \mathbf{dS} + \int_\Omega \rho \mathbf{G} dV,$$

ACCEPTED MANUSCRIPT

where **dS** is the unit normal vector on the body surface, $\bar{\bar{\tau}}$ is the stress tensor defined as $\tau_{ij} = \nu\rho\left(\frac{\partial u_i}{\partial x_j} + \frac{\partial u_j}{\partial x_i}\right)$ for a Newtonian fluid, and **G** is the external force field.

If the immersed body moves with a velocity $\mathbf{u_s}$, the contribution of the internal or virtual flow, namely the unsteady flow inside the body domain, should be taken into account when calculating the total force $\mathbf{F_{mov}}$. Following Reference [40], it is found that:

$$\mathbf{F_{mov}} = \mathbf{F_{stat}} + \rho \int_{\Omega_b} \frac{\partial \mathbf{u_s}}{\partial t} dV.$$

Acknowledgement

The financial support of the European Commission through the PELskin FP7 European project (AAT.2012.6.3-1.- Breakthrough and emerging technologies) is acknowledged.

References

[1] J. Masliyah, M. Polikar, Terminal velocity of porous spheres, T. Can. J. Chem. Eng. 58 (1980) 299 – 302.

[2] P. Noymer, L. Glicksman, A. Devendran, Drag on a permeable cylinder in steady flow at moderate Reynolds numbers, Chem. Eng. Sci. 53 (1998) 2859 – 2869.

[3] S. Bhattacharyya, S. Dhinakaran, A. Khalili, Fluid motion around and through a porous cylinder, Chem. Eng. Sci. 61 (2006) 4451 – 4461.

[4] C.-H. Bruneau, I. Mortazavi, Passive control of the flow around a square cylinder using porous media, Int. J. Numer. Meth. Fl. 46 (2004) 415 – 433.

[5] C.-H. Bruneau, I. Mortazavi, Numerical modelling and passive flow control using porous media, Comput. Fluids 37 (2008) 488 – 498.

[6] C. Brücker, C. Weidner, Influence of self-adaptive hairy flaps on the stall delay of an airfoil in ramp-up motion, J. Fluid. Struct. 47 (2014) 31 – 40.

[7] Z. Guo, C. Shu, Advances in Computational Fluid Dynamics - Vol.3 - Lattice Boltzmann Method and its Applications in Engineering, World Scientific Publishing Co. Pte. Ltd., 2013.

[8] O. Dardis, J. McCloskey, Lattice Boltzmann scheme with real numbered solid density for the simulation of flow in porous media., Phys. Rev. E 57 (1998) 4834–4837.

[9] M. Spaid, F. Phelan, Lattice Boltzmann methods for modeling microscale flow in fibrous porous media, Phys. Fluids 9 (1997) 2468–2474.

ACCEPTED MANUSCRIPT

[10] X. Shan, G. Doolen, Multicomponent Lattice-Boltzmann Model with Interparticle Interaction, J. Stat. Phys. 81 (1995) 379 – 393.

[11] P. Nithiarasu, K. N. Seetharamu, T. Sundararajan, Natural convective heat transfer in a fluid saturated variable porosity medium, Int. J. Heat Mass Tran. 40 (16) (1997) 3955 – 3967.

[12] Z. Guo, T. S. Zhao, Lattice Boltzmann model for incompressible flows through porous media, Phys. Rev. E 66 (2002) 036304.

[13] L. Wang, L.-P. Wang, Z. Guo, J. Mi, Volume-averaged macroscopic equation for fluid flow in moving porous media, Int. J. Heat Mass Tran. 82 (2015) 357 – 368.

[14] C. Peskin, Numerical Analysis of Blood Flow in the Heart, J. Comput. Phys. 25 (1977) 220 – 252.

[15] J. Wu, C. Shu, Implicit velocity correction-based immersed boundary-lattice Boltzmann method and its applications, J. Comput. Phys. 228 (2009) 1963 – 1979.

[16] D.-J. Chen, K.-H. Lin, C.-A. Lin, Immersed boundary method based lattice Boltzmann method to simulate 2D and 3D complex geometry flows, Int. J. Mod. Phys. C 18 (2007) 585 – 594.

[17] S. Kang, Y. Hassan, A comparative study of direct-forcing immersed boundary-lattice Boltzmann methods for stationary complex boundaries, Int. J. Numer. Meth. Fl. 66 (2011) 1132 – 1158.

[18] J. Favier, A. Revell, A. Pinelli, A Lattice Boltzmann-Immersed Boundary method to simulate the fluid interaction with moving and slender flexible objects, J. Comput. Phys. 261 (2014) 145 – 161.

[19] Y. Kim, C. Peskin, 2D Parachute Simulation by the Immersed Boundary Method, SIAM J. Sci. Comput. 28 (2006) 2294 – 2312.

[20] J. Stockie, Modelling and simulation of porous immersed boundaries, Comput. Struct. 87 (2009) 701 – 709.

[21] D. Natali, J. Pralits, A. Mazzino, S. Bagheri, Stabilizing effect of porosity on a flapping filament, J. Fluid. and Struct. 61 (2016) 361 – 375.

[22] Z. Guo, C. Zheng, B. Shi, Discrete lattice effects on the forcing term in the lattice Boltzmann method, Phys. Rev. E 65 (2002) 046308.

[23] E. Fadlun, R. Verzicco, P. Orlandi, J. Mohd-Yusof, Combined Immersed-Boundary Finite-Difference Methods for Three-Dimensional Complex Flow Simulations, J. Comput. Phys. 161 (2000) 35 – 60.

ACCEPTED MANUSCRIPT

[24] Z.-G. Feng, E. Michaelides, The immersed boundary-lattice Boltzmann method for solving fluid-particles interaction problems, J. Comput. Phys. 195 (2004) 602 – 628.

[25] X. Niu, C. Shu, Y. Chew, Y. Peng, A momentum exchange-based immersed boundary-lattice Boltzmann method for simulating incompressible viscous flows, Phys. Lett. A 354 (2006) 173 – 182.

[26] A. Pinelli, I. Naqavi, U. Piomelli, J. Favier, Immersed-boundary methods for general finite-difference and finite-volume Navier-Stokes solvers, J. Comput. Phys. 229 (2010) 9073 – 9091.

[27] A. Roma, C. Peskin, M. Berger, An Adaptive Version of the Immersed Boundary Method, J. Comput. Phys. 153 (1999) 509 – 534.

[28] Q. Zou, X. He, On pressure and velocity boundary conditions for the lattice Boltzmann BGK model, Phys. Fluids 9 (1997) 1591 – 1598.

[29] Q. Lou, Z. Guo, B. Shi, Evaluation of outflow boundary conditions for two-phase lattice Boltzmann equation, Phys. Rev. E 87 (2013) 063301.

[30] P. Yu, Y. Zeng, T. Lee, X. Chen, H. Low, Steady flow around and through a permeable circular cylinder, Comput. Fluids 42 (2011) 1 – 12.

[31] G. Koopmann, The vortex wakes of vibrating cylinders at low Reynolds numbers, J. Fluid Mech. 28 (1967) 501 – 512.

[32] C. Williamson, Vortex dynamics in the cylinder wake, Ann. Rev. Fluid Mech. 28 (1996) 477 – 539.

[33] X.-Y. Lu, C. Dalton, Calculation of the timing of vortex formation from an oscillating cylinder, J. Fluid. Struct. 10 (1996) 527 – 541.

[34] M. Uhlmann, An immersed boundary method with direct forcing for the simulation of particulate flows, J. Comput. Phys. 209 (2005) 448 – 476.

[35] J. Yang, E. Balaras, An embedded-boundary formulation for large-eddy simulation of turbulent flows interacting with moving boundaries, J. Comput. Phys. 215 (2006) 12 – 40.

[36] M. Nobari, H. Naderan, A numerical study of flow past a cylinder with cross flow and inline oscillation, Comput. Fluids 35 (2006) 393 – 415.

[37] A. Placzek, J.-F. Sigrist, A. Hamdouni, Numerical simulation of an oscillating cylinder in a cross-flow at low Reynolds number: Forced and free oscillations, Comput. Fluids 38 (2009) 80 – 100.

[38] M.-C. Lai, C. Peskin, An Immersed Boundary Method with Formal Second-Order Accuracy and Reduced Numerical Viscosity, J. Comput. Phys. 160 (2000) 705 – 719.

ACCEPTED MANUSCRIPT

[39] R. Mei, D. Yu, W. Shyy, L.-S. Luo, Force evaluation in the lattice Boltzmann method involving curved geometry, Phys. Rev. E 65 (2002) 041203.

[40] L. Shen, E.-S. Chan, P. Lin, Calculation of hydrodynamic forces acting on a submerged moving object using immersed boundary method, Comput. Fluids 38 (2009) 691 – 702.

ACCEPTED MANUSCRIPT